Advances in Materials Science

Chapter 1

Novel Ni-Based Alloy with Both High Strength and High Corrosion Resistance

***Li Yunping*[1*], *Yang Biaobiao*[1], *Qing Liu*[2]**

[1]*State Key Lab for Powder Metallurgy, Central South University, Changsha, China*

[2]*Yuanmeng Precision Technology (Shenzhen) Institute, Shenzhen, China*

[*]***Correspondence to: Li Yunping,*** *State Key Lab for Powder Metallurgy, Central South University, Changsha, China. Fax: +86-731-8887-6692; Email: lyping@csu.edu.cn*

Abstract

The development of novel Ni-based alloys combining with both excellent mechanical performance and higher corrosion resistance is of great importance for their applications in severe environments such as molten salt reactor, etc.. In this chapter, by dual-alloying of both Co and Cu to the commercial NiCrMo alloy, a novel Ni-based alloy with outstanding mechanical performance and superior corrosion resistance to HF acid solution is developed. Further cold working and aging treatments can help boost the mechanical strength without lowering the corrosion resistance to HF acid solution, owing to exceptional stability of metallic Cu passive film. Detailed description regarding the alloy designing strategy, strengthening mechanism, and passivation mechanism of alloy in HF acid solution is given systematically in this work.

Keywords: NiCoCrMoCu alloy; Corrosion behavior; HF acid environment; Mechanical properties; Dual-alloying

1. Introduction

Rapid developments of industry and technology require the materials with more and more exceptional properties, given many traditional alloys cannot perform well owing to the more severe servicing environments in some cases. Taking the molten salt reactor experiment (MSRE) conversion project for an example, this project involves converting ^{233}U to a stable oxide, and a global reaction of conversion process can be summarized as follow[1]:

$$UF_6 + 3H_2O \rightarrow UO_3 + 6HF \qquad (1)$$

Where 6 moles of HF are produced from the reaction of each mole of UF_6, suggesting a concentrated hydrofluoric acid aqueous (HF) solution will be formed in the hydrolysis process of uranium hexafluoride. HF acid is extremely corrosive to most common alloys including Ni-based alloys. In this reaction, a barrel is needed to contain and transfer the resultant HF acid [2]. For the barrel materials, the superior performance of both corrosion resistance to the HF acid solution and comprehensive mechanical properties are required concurrently. Similar condition can be also found for the screw materials in injection moulding machine for fluorine-containing resins or plastics like polyfluoroalkoxy (PFA) [3,4]. In this case, HF acid aqueous solution will be formed due to the decomposition of PFA at high temperature. This means a high corrosion resistance to HF acid solution of screw materials is necessary. In addition, the working screws components will suffer from high friction and wear to ensure flow of resins or plastics. Thus, very superior mechanical performances such as hardness are also required for screws materials. Unfortunately, due to their lower mechanical performance, the commercial Hastelloy (Ni-Cr-Mo) alloys cannot simultaneously meet these several requirements. A new alloy with both higher strength and higher corrosion resistance is imperative to be developed.

A large number of works on designing novel alloy with higher strength, higher corrosion resistance, etc. have been conducted, and various designing strategies including alloying, working, aging, surface treatment etc. have been used extensively [5–11]. Taking Ni-based alloys for an example, by alloying of cobalt element, Ni-Co-based alloys were developed by Yuan et al., suggesting that higher Co-containing TMW-4M3 alloy shows higher tensile strength and more superior creep resistance compared to commercial U720Li alloy, owing to lower stacking faults energy and altered deformation mechanism from slip-dominated to twin-dominated after the addition of Co [12,13]. Similar Co strengthening behavior can also be found in other Ni-based alloys[14,15]. In addition, Cu addition has been affirmed effective to improve the corrosion resistance of alloys [16–24]. In the works of Yang et al., the addition of Cu to Ni-Co-Cr-Mo alloy can suppress the anodic reaction, postpone the oxidation behavior of Cr(III), and stabilize Mo-rich passive film at high voltage in neutral chloride condition[25]. Their further electrochemical analysis in acidic chloride solution show a different role of Cu, where suppressed cathodic and anodic reactions by Cu addition is observed [26]. Moreover,

Cu has been determined to be beneficial to improve the corrosion resistance of Ni-based alloy in wet HF surroundings [27,28].

Alloying, working and aging treatments are also beneficial to improve the mechanical property of Ni-based alloy. By cold working, numerous dislocations can be introduced, giving rise to work hardening by impeding the further dislocation motions. Introducing dispersive precipitate by aging is another common and effective method to improve the mechanical performance of alloy. By proper thermal treatments, second phase precipitates could be formed in the matrix. These particles act like pinning sites to impede the movement of dislocations. During practical deformation of precipitate-containing alloy, dislocations cutting through the particles or by looping mechanism depends strongly on the particle size, the interface coherency, the nature of matrix and particles, etc.[29,30]. For example, the interaction of dislocations and smaller particles could cut through the particles; while for larger particles, the dislocations will tend to loop or bow to overcome the obstacles. The commercial age-hardening IN718 (UNS N07718/W.Nr. 2.4668) alloy could precipitate face-centered cubic coherent γ′ phase (Ni_3Al), metastable body centered tetragonal coherent γ′′ phase (Ni_3Nb), and orthorhombic incoherent δ phase (Ni_3Nb). To control the precipitation behavior of IN718 alloy is still a hot topic to boost the mechanical performance of IN718[31,32].

In this chapter, a novel Ni-30Co-16Cr-15Mo-2Cu alloy combining with high strength and excellent corrosion resistance in hydrofluoric acid solution was introduced and its designing strategy will be also depicted by theoretical calculations and experimental measurements systemically.

2. Methods

2.1. Materials

The alloys investigated in this chapter have nominal compositions of Ni-16Cr-15Mo-6Fe (NiCrMo, wt.%), Ni-30Co-16Cr-15Mo-6Fe alloy (NiCoCrMo, wt.%) and Ni-30Co-16Cr-15Mo-6Fe-2Cu (NiCoCrMoCu, wt.%). All ingots were fabricated by vacuum melting, and subjected to homogenization treatment at 1250°C for 12 h. Some specimens were further subjected to hot forging or cold forging with 30%, 60%, or 90% reduction rates using a 300 Ton hydraulic servo presser (EFP-300H, Asai Corporation, Japan). The hot forging was followed by air cooling. Then, some specimens were aged at 600°C for 1 h (A state). The nomination of samples is based on what kinds of treatments having applied on the samples. For example, if a NiCoCrMoCu sample was subjected to 90% cold forging and further aging treatment, the nomination of such sample should be NiCoCrMoCu-Cold90A; meanwhile, NiCrMo, NiCoCrMo, and NiCoCrMoCu samples represent corresponding alloys after homogenization treatment while without any deformation or aging treatments.

2.2. Microstructure characterization

The initial microstructures of samples were characterized using electron backscatter diffraction (EBSD) analysis system that was loaded with data acquisition software (TSL-OIM 5.0, TexSEM Laboratories, Inc., Provo, UT). The EBSD measurements were performed using a field-emission scanning electron microscope (FEI XL30S, FEI Company, Portland, OR), which was operated at an accelerating voltage of 20 kV. The measurements were performed at a step size of 1.0 μm.

The surface profiles of the samples before and after the immersion test were observed using laser scanning microscopy (LSM) system (VK-X200 series, Keyence, Japan) with a resolution of 48.83 nm across the surface and a height resolution of 0.1 nm.

XPS (Axis ultra DLD, Kratos) analysis of the immersed samples was performed to obtain the depth profiles of the passive films. The beam and spot sizes used in the XPS measurements were 300 × 700 μm^2 and 2 mm (diameter), respectively. Step sizes of 1 and 0.1 eV were used in the survey scan and regional scan, respectively. The sweep time was approximately 10 in each regional scan.

TEM characterization was performed using a JEOL JEM-2100F microscope equipped with double spherical aberration correctors for both the probe-forming and image-forming lenses (CEOS, CESCOR, and CETCOR). High-angle annular dark field (HAADF) scanning transmission electron microscope (STEM) images were acquired using an annular-type STEM detector with an angle ranging from 100 to 267 mrad. Thin films of the immersed alloy specimens were cut using a combined scanning electron microscopy (SEM)/focused ion beam (FIB) system (Quanta 3D and Helios Dual-Beam NanoLab, FEI) for cross-sectional TEM observations. A thin protective carbon layer was deposited on the area of interest across the slip traces before the FIB process.

2.3. Corrosion and mechanical tests

For the immersion tests in aqueous HF acid solution, the samples were cut into small pieces (20 × 20 × 1 mm^3) and grounded with SiC abrasive paper, followed by being polished with 1 and 0.3 μm alpha alumina suspension (AP-A suspension, Struers, Tokyo). Finally, after being cleaned in ethanol using an ultrasonic cleaner and dried with a blower, mirror-polished samples were obtained for immersion tests. Since the corrosion of alloys by HF acid gas during the injection molding process is preceded mostly by a chemical reaction of the alloy elements with the HF acid gas, we used the immersion test and not the electrochemical method to evaluate the corrosion resistances of the tested alloys. The apparatus for the immersion tests can be seen in our previous studies[33,34]. There are no data available on the actual concentration of HF acid gas during the injection moulding process. In the present study,

an aqueous HF acid solution with a concentration (approximately 5.2 M) much higher than the actual one was used in order to investigate the corrosion resistance of these alloys in an accelerated manner. This solution was prepared by mixing HF acid (46%) (JIS K 8819, Morida Chemical Industry Co. LTD, Osaka) with distilled water in the draft chamber. For each test, approximately 40 ml of this solution was added to a Teflon crucible enclosed in a stainless-steel vessel. This vessel was then placed in an electric oven, which was placed in a draft chamber for the purposes of removing any leaking HF gas. The prepared samples were then individually immersed in the HF acid solution at 100°C by being suspending from a Teflon wire. This ensured that the contact area between sample and the vessel was negligibly small. A K-type thermocouple covered with a close-ended alumina tube was used to monitor the temperature. The mirror-polished samples were immersed individually in the HF acid solution at 100°C. After being immersed for a given period, which ranged from 1 to 100 h, the sample was removed and washed ultrasonically for 1 min in distilled H_2O. It was then dried in a drying cube for approximately 10 min at the ambient temperature. The dried sample was then used for microstructural observations and corrosion rate measurements.

The hardness of each sample was measured 10 times using a Vickers hardness tester (Shimazu, HMV) with a load of 1 kg. For tensile tests, the nominal dimensions of the gauge section of the specimens were 11 mm long, 2 mm wide, and 1.5 mm thick. Specimens were cut out by using electro discharge machining (EDM) and its surface was mechanically polished to P #800 grit SiC paper. Tensile tests were performed using an INSTRON 8562 electro-mechanical testing machine in air environment at room temperature (approximately 25℃) with a constant stroke rate of 0.1 mm/min.

3. Results and Discussion

In this study, various factors, including alloying compositions, heat treatments, deformation procedures, aging treatment, etc., are considered systematically during the design of NiCoCrMoCu alloy. We will firstly introduce NiCoCrMo alloy with 30 wt.% Co addition to commercial NiCrMo alloy, and explore the influence of Co on the microstructure, corrosion behavior and mechanical performance of NiCrMo alloy. Then, on the basis of NiCoCrMo alloy, we further investigate the impact of extra 2 wt.% Cu addition on the structure and performance of NiCoCrMo alloy. The roles of other factors including deformation treatments, aging treatment, etc. are interlaced along with the principal line.

3.1. Substantial substitution of Co to Ni

3.1.1. Phase diagram of Ni-16Cr-15Mo(-xCo) alloys

Phase constitution of alloy takes a significant role on the mechanical performance and corrosion behavior of alloy. Thus, the consideration of phase diagram is imperative to

alloy design. The phase diagram of Ni-16Cr-15Mo(-xCo) alloys has been calculated using a commercial thermodynamic calculation software Thermo-Calc 5.0, TCW (Thermo-Calc Software, Stockholm, Sweden) on the basis of Ni-based alloy database, as shown in **Figure 1** [35]. From the calculated result, face centered cubic (FCC) γ phase turns gradually instable with the increase of Co content. Moreover, with the increasing of Co concentration, below approximately 1070°C, the second phase π phase with tetragonal crystalline structure in the NiCrMo alloy was all replaced by a hexagonal μ phase in the NiCoCrMo alloy.

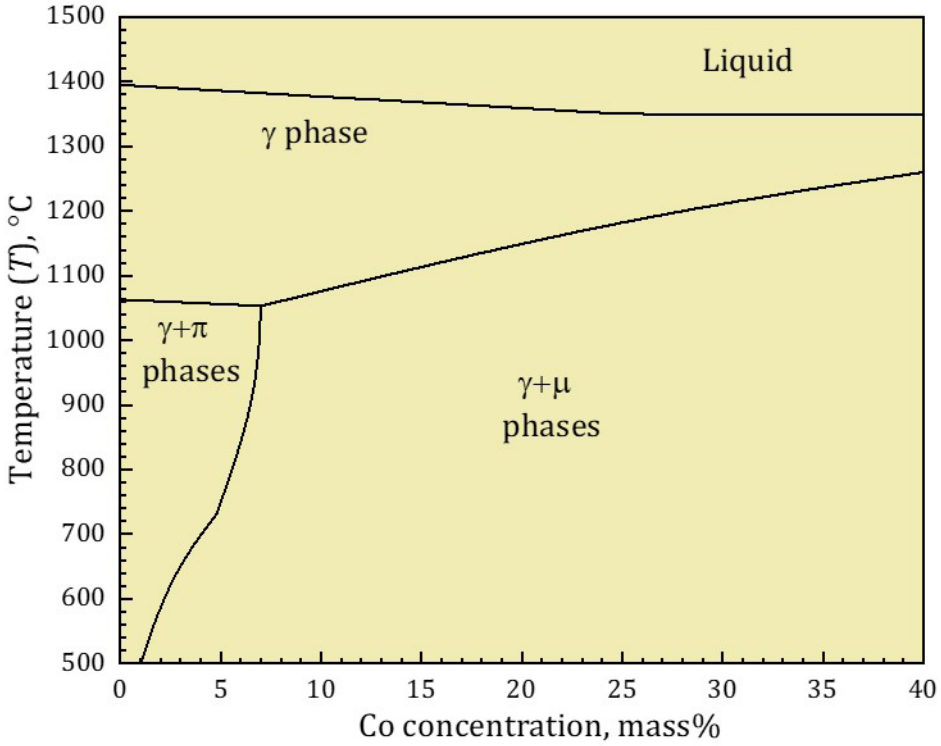

Figure 1: The phase diagram of Ni-16Cr-15Mo(-xCo) alloys.

3.1.2. Initial microstructure characterization

The inverse polar figure (IPF) and kernel average misorientation (KAM) maps for NiCrMo and NiCoCrMo alloys after cold compression to reduction rates of 0%, 30%, and 60%, obtained through EBSD analysis, are shown in **Figure 2**. Both alloys without compression exhibit a completely annealed microstructure, as evidenced by the large number of annealing twins. The mean grain sizes of the two defect-free alloys are determined to be approximately 300 μm. After 30% compression, the grains of both alloys deform slightly (**Figure 2** (**b1**, **e1**)) and exhibit a gradual variation in the orientation of their interiors. Upon further compression, the initially large grains are gradually divided into smaller ones by both LABs and high-angle boundaries (HABs) or mechanical twin boundaries (**Figure 2** (**c1**, **f1**)). This is indicative of the grain refining effect resulting from the cold working. Correspondingly, the kernel average misorientation (KAM) maps of these samples also exhibit a nonuniform distribution, and the degree of nonuniformity increases significantly with the increase of compression reduction rate (**Figure 2** (**a2**-**f2**)). Note that, under the same compression reduction rates (30% or 60%), compared to the grains of NiCrMo alloy, those of NiCoCrMo alloy seem to be more heavily

distorted. The more severe distortion in the grains of NiCoCrMo alloy can be also clearly seen from corresponding KAM maps.

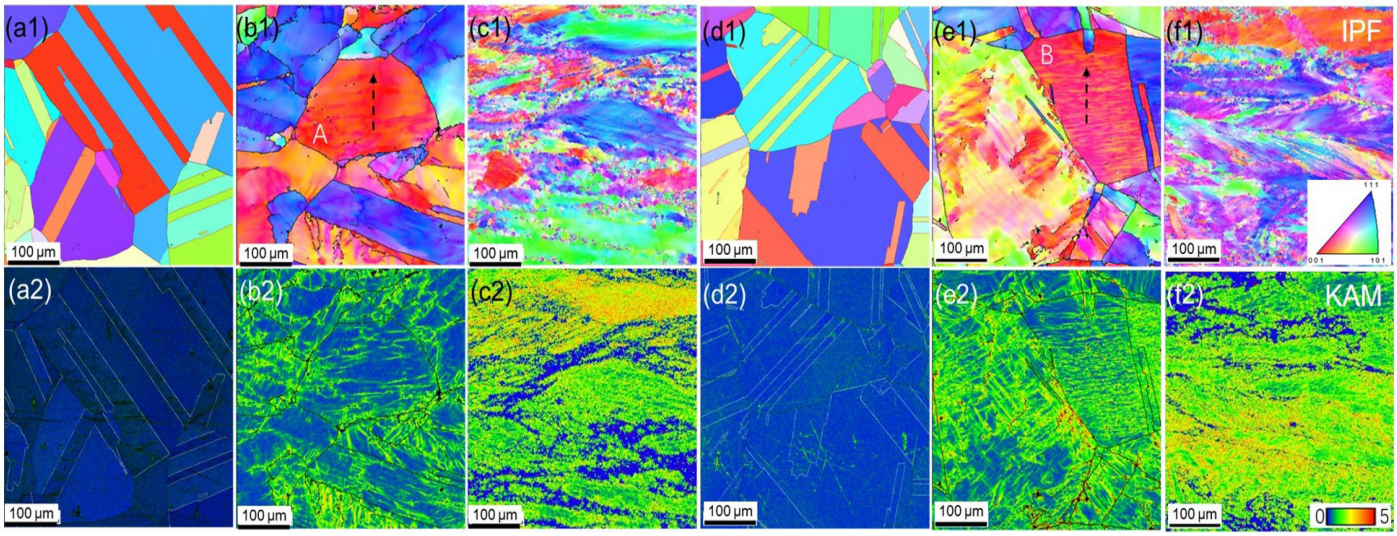

Figure 2: (a1–f1) Inverse pole figure (IPF) maps and (a2-f2) kernel average misorientation (KAM) maps of (a-c) NiCrMo and (d-f) NiCoCrMo alloys cold forged to (a and d) 0%, (b and e) 30%, and (c and f) 60%, respectively. Reprinted from ref.[33], with kind permission from Elsevier.

3.1.3. Performances of NiCrMo and NiCoCrMo alloys

The hardness of NiCrMo and NiCoCrMo alloys subjected to various reduction rates of compression treatments are shown in **Figure 3**. Evidently, there is a significant increase in the hardness of both alloys after compression. After compression reductions of 0%, 30%, and 60%, the hardness of NiCoCrMo alloy is 10%, 19%, and 4.3%, respectively, higher than that of NiCrMo alloy. This suggests that Co addition plays a significant role in enhancing the work hardening rate of alloy.

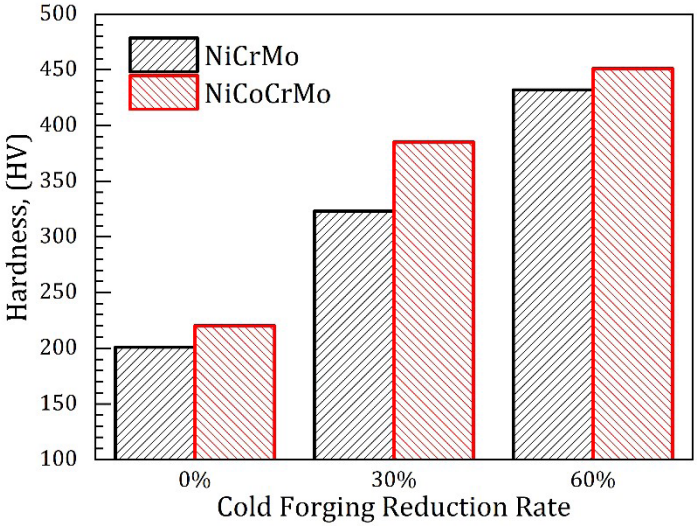

Figure 3: Hardness results of NiCrMo and NiCoCrMo alloys as a function of reduction rate. Reprinted from ref.[33], with kind permission from Elsevier.

The mass losses of the NiCrMo and NiCoCrMo alloys subjected to various compression reduction rates as functions of the immersion time are shown in **Figure 4** (a) and (b), respectively. The mass losses of the uncompressed samples of the two alloys are comparable for a given immersion time, with their curves, which are parabolic, exhibiting almost similar behavior as

the immersion time is increased. After immersion for 100 h, the mass losses of the NiCrMo and NiCoCrMo samples are almost similar and approximately 3.6 mg/cm^2 and 5.8 mg/cm^2, respectively. Under similar immersion for 100 h, the mass losses of the NiCoCrMo-Cold30 and NiCoCrMo-Cold60 samples are approximately 32 mg/cm^2 and 45 mg/cm^2, respectively, indicating the cold-working process results in a significant decrease in the corrosion resistance of NiCoCrMo alloy. In addition, from current tendency, these values are assumed to be increased greatly with further immersion, which is in contrast to the uncompressed NiCoCrMo alloy demonstrating a parabolic behavior. In contrast, the mass losses of the NiCrMo alloys compressed by 30% and 60% are 4.7 mg/cm^2, and 5.8 mg/cm^2, respectively. These values are slightly higher than those of the uncompressed NiCrMo samples, but much lower than those of the NiCoCrMo samples after compression.

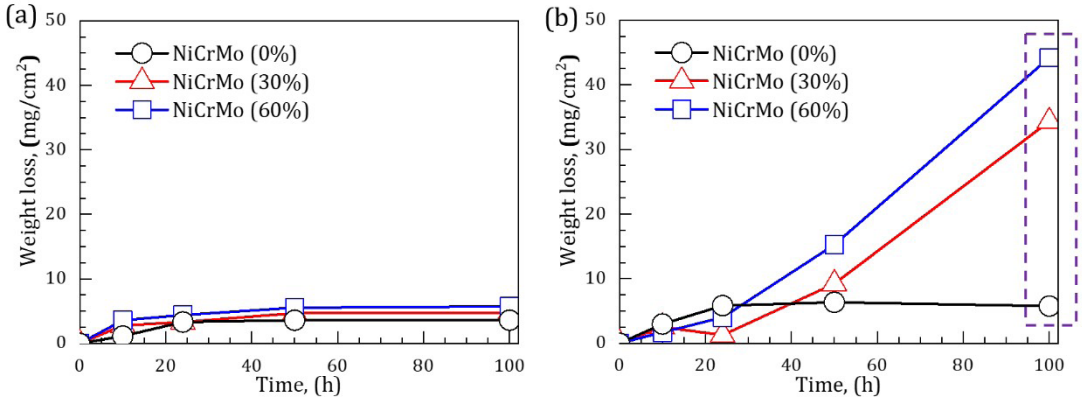

Figure 4: Weight losses of (a) NiCrMo alloy and (b) NiCoCrMo alloy compressed to 0%, 30%, and 60% after immersion in 5.2 M HF acid aqueous solution for various durations at 100°C.

3.1.4. Calculated SFE

It is well known that deformation behavior of metallic materials strongly depends on strain, strain rate, deformation temperature, and the nature of materials, which to some extent can be expressed in terms of the stacking fault energy (SFE) [36–38]. In this chapter, the SFE of NiCrMo and NiCoCrMo alloys are estimated using Olson and Cohen method based on the thermo dynamical calculation of an FCC structure transition to an HCP structure [39,40]. The equation containing the sum of a volumetric energy term and a surface energy term is given by

$$\gamma = 2\rho\Delta G^{\gamma\to\varepsilon} + 2\sigma^{\gamma/\varepsilon} \qquad (2)$$

in which $\Delta G^{\gamma\to\varepsilon}$ and $\sigma^{\gamma/\varepsilon}$ are the Gibbs energy difference and the interface energy between γ and ε phases, respectively. ρ is the atomic density of the $\{111\}_\gamma$ plane per mole, which can be defined as

$$\rho = \frac{4}{\sqrt{3}}\frac{1}{\alpha^2 N} \qquad (3)$$

It should be noted that the lattice constant α is obtained by calculation of diffraction

pattern[41]. All alloys use an identical value of α for calculation considering the elemental volumetric ratio among Co, Ni, and Cu being close to unity. The interfacial energy term $2\sigma^{\gamma/\varepsilon}$ is assumed to be 15 $mJ \cdot m^{-2}$[42]. The other thermodynamic data needed are obtained from the Thermo-Calc software[35]. The results of the SFE calculation are shown in **Figure 5**. Clearly, NiCoCrMo alloy exhibits lower SFE compared to NiCrMo alloy, which is in agreement with prior researches [43–46]. Note SFE is an important factor influencing the hot working behavior of alloy and subsequent microstructure. Lower SFE makes alloy more feasible to deform through forming a larger number of split dislocations and stacking faults, as well as deformation twins. Unlike the unstable twin boundaries in high-SFE materials, these defects, especially the twin boundaries and stacking fault bands, are very stable and can block mobile dislocations, accommodate plastic deformation by storing dislocations, and migrate under stresses, thus enhancing the hardness and strength, even plasticity[47–49].

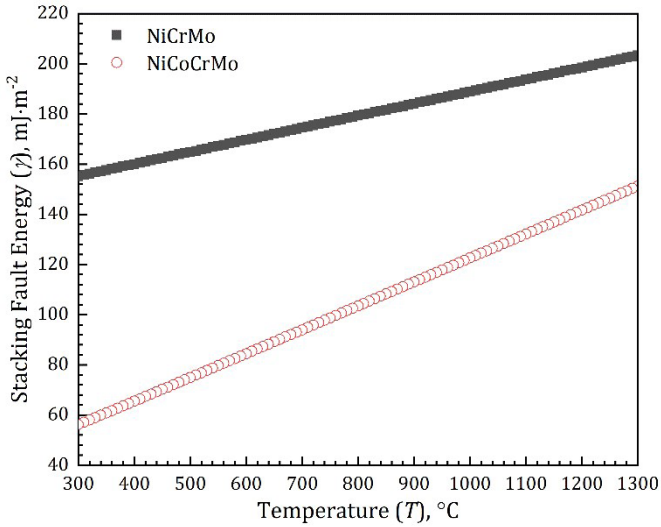

Figure 5: Calculated SFE of NiCrMo and NiCoCrMo alloys as a function of temperature.

3.1.5. Corrosion morphologies of NiCrMo and NiCoCrMo alloys

Figure 6 shows the surface morphologies and the surface height distributions along the horizontal dashed lines of the (a) NiCrMo and (b) NiCoCrMo alloys with a reduction rate of 60%. At a compression reduction of 60%, both alloys exhibit stronger peaks in their surface-height distributions, indicating more significant selective dissolution owing to cold working. NiCrMo sample compression reduced by 60% and immersed in the HF acid solution shows pronounced slipping bands. It should be noted that, compared to the NiCrMo-Cold60 sample (**Figure 6** (**a**)), the NiCoCrMo-Cold60 sample (**Figure 6** (**b**)) exhibits much rougher surfaces, and the peaks corresponding to the deformed areas within their grains are stronger, owing to the fact that these areas react preferentially with the HF acid solution. For example, the difference in the heights of the maximum and minimum peaks in the case of NiCrMo-Cold60 sample is approximately 4.5 μm, which is 40% of that for NiCoCrMo-Cold60 sample (approximately 11 μm), as measured from the height distributions shown in **Figure 6** (**a**) and (b), respectively.

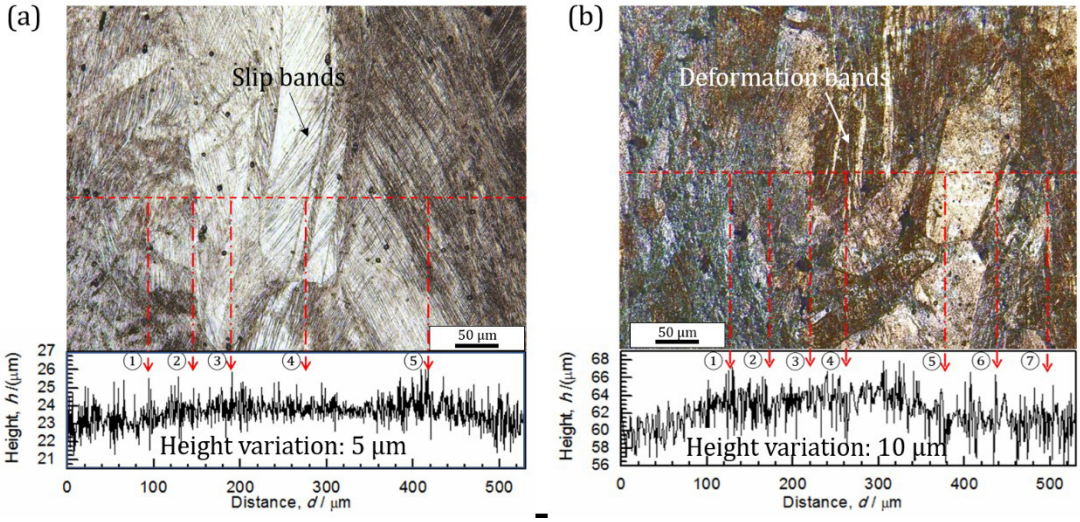

Figure 6: Surface morphologies and corresponding height distributions of the sample surface along the horizontal dashed line in (a) NiCrMo-Cold60, and (b) NiCoCrMo-Cold60 samples after immersion in 5.2 M HF acid aqueous solution at 100°C for 100 h. Reprinted from ref.[33], with kind permission from Elsevier.

To further investigate the effects of plastic deformation on the corrosion resistance of both NiCrMo and NiCoCrMo alloy in HF acid, both alloys are conducted a prior deformation by hardness tester with a square base pyramidal indenter and their corrosion behaviors are then quantitatively evaluated using a newly developed laser microscope.

The initial microstructure of the two alloy samples, as observed by EBSD (**Figure 7**), shows two grains with identical orientations close to the <101> direction, as indicated by the black arrows in **Figure 7** (**a**) and (**b**). These two particular grains are selected for subsequent indentation testing, since grains with different orientations would exhibit very different behavior even under the same deformation condition. The microstructures of the two samples after indentation testing, again observed by EBSD analysis, are shown in terms of image quality (IQ) maps in **Figure 7** (**c-d**). Slip bands along the {111} planes are extensively observed around the indentation, which is indicative of plastic deformation in the matrix of both alloys. More severe plastic deformation is evident inside the indentation itself, as characterized by the higher density of slip bands. Owing to the higher hardness of NiCoCrMo, the width of its indentation is slightly less than that of NiCrMo, implying that the NiCrMo is subjected to more severe plastic deformation in the interior of its indentation.

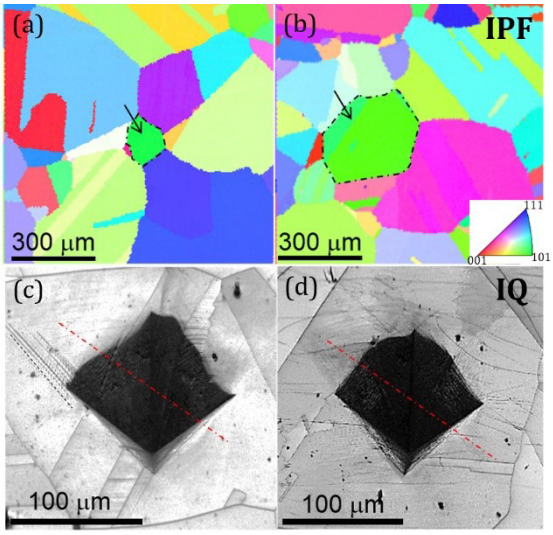

Figure 7: (a-b) IPF maps and (c-d) image quality (IQ) maps of (a, c) NiCrMo and (b, d) NiCoCrMo alloys: where are the microstructure (a-b) prior to indentation and (c-d) after indentation. Reprinted from ref.[50], with kind permission from Elsevier.

To provide a quantitative evaluation of the variation in indentation geometry with immersion, the height distribution across the center of indentation in the NiCrMo and NiCoCrMo alloys (shown by the dashed lines in **Figure 8** (**c-d**)) is plotted in **Figure 8** (**a**) and (**b**), respectively. We can see from this that with prolonged immersion, the width and depth of the indentation in both alloys are enlarged to a certain degree due to dissolution of the indentation interior. In the case of NiCrMo, the initial depth of indentation prior to immersion is approximately 21 μm, while the final depth after immersion for 20 h is approximately 31 μm, clearly indicating dissolution of the alloy matrix. In contrast, even though the initial depth of the NiCoCrMo alloy indentation is only slightly less than that of the NiCrMo alloy at approximately 18 μm, the final depth after immersion for 20 h of 42 μm is much greater. This implies that the rate of dissolution of NiCoCrMo in HF acid is more sensitive to plastic deformation. Moreover, the dissolution of NiCrMo alloy occurs in a more parallel direction, by expanding the width of the indentation.

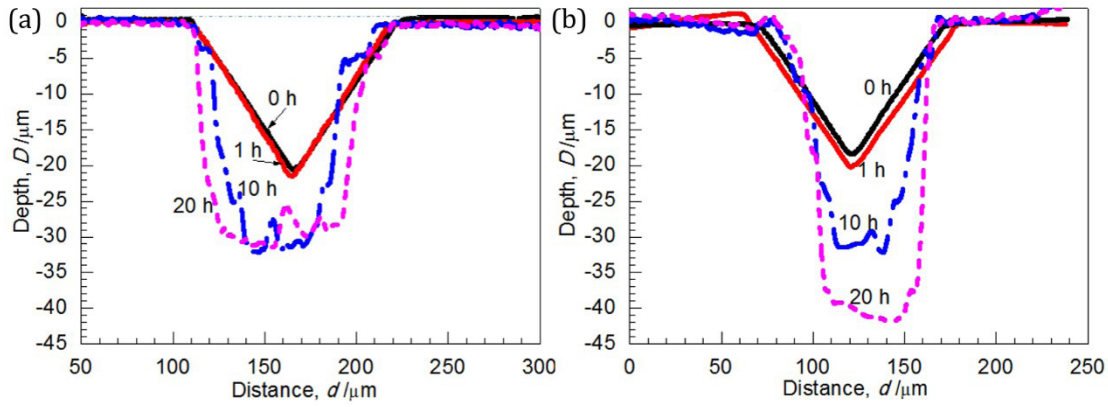

Figure 8: Height distribution across the center of indentation of (a) NiCrMo and (b) NiCoCrMo alloys after immersion in HF acid aqueous solution (5.2 M) at 100°C for various durations. Reprinted from ref. [50], with kind permission from Elsevier.

3. 1. 6. Model of interface corrosion behavior with Co added

Based on existing results and other studies on NiCoCrMo alloys, a proposed mechanism to explain the passive film formation on the surface of the NiCoCrMo alloy in (5.2 M) HF acid solution at 100°C, which can be seen in **Figure 9**[16,51]. Firstly, when the specimen contacts the HF acid solution, the surface of the alloy is selectively dissolved through general corrosion attack (**Figure 9** (**a**)). Consequently, the solution becomes enriched in Cr^{3+}, Ni^{2+}, and Co^{2+} species, whereas the material surface is enriched in Mo^{x+} (x=4, 5, 6) (**Figure 9** (**b**)), as demonstrated by Hou et al.[16]. In the final step, Mo forms a compact and protective layer of $MoO_{x/2}$ with a small fraction of Ni^{2+} and Co^{2+} in forms of fluorides or oxides (**Figure 9** (**c**)), revealed by Li et al. [51]. There is no essential difference between the passive mechanisms of the NiCrMo and NiCoCrMo alloys.

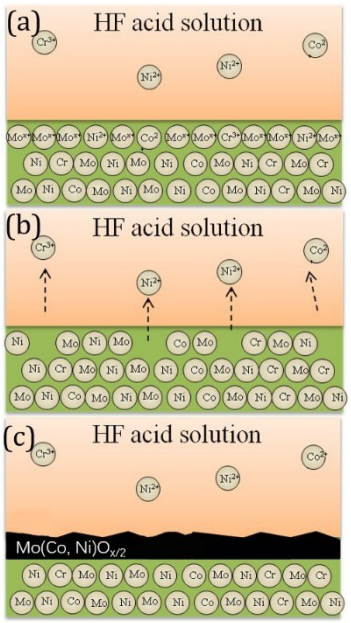

Figure 9: Corrosion mechanism proposed for NiCoCrMo alloy in HF acid aqueous solution: (a) selective dissolution of Ni, Cr and Co in alloy surface, (b) Mox+ enrichment on the sample surface, and (c) formation of compact MoOx/2 protective layer. Reprinted from ref. [34], with kind permission from Elsevier.

3.2. Influence of further 2 mass% Cu addition

3.2.1. Phase diagram of Ni-30Co-16Cr-15Mo(-xCu) alloys

Figure 10 shows the phase diagram of Ni-30Co-16Cr-15Mo(-xCu) alloys. Similar to the calculation of Ni-16Cr-15Mo(-xCo) alloys phase diagram, this phase diagram were also calculated using a commercial thermodynamic calculation software Thermo-Calc 5.0, TCW (Thermo-Calc Software, Stockholm, Sweden) on the basis of Ni-based alloy database[35]. From **Figure 10**, with Cu concentration increasing, the transform temperatures of liquid phase to face centered cubic (FCC) γ phase, and FCC γ phase to hexagonal μ phase turns gradually declined. In contrast, the temperature to precipitate σ phase seems increased with Cu concentration increasing, suggesting a higher fraction of Cu is considered likely to induce a Mo-rich σ phase.

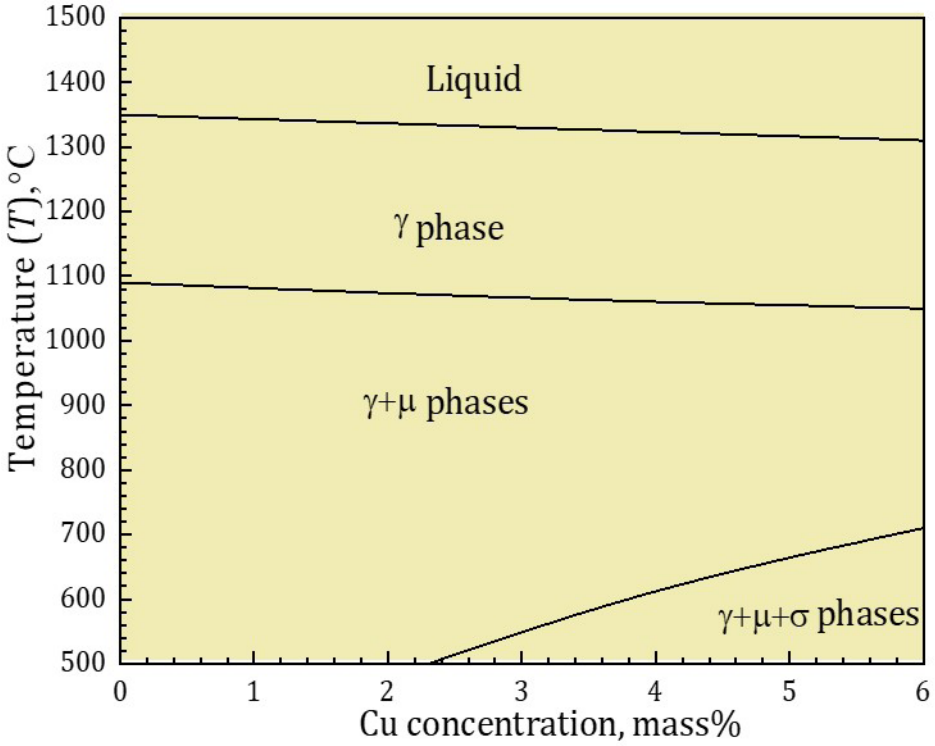

Figure 10: The phase diagram of Ni-30Co-16Cr-15Mo(-xCu) alloys.

3.2.2. Initial microstructure characterization

The microstructural observations performed by EBSD are illustrated by the image quality (IQ) maps in **Figure 11** (**a1-c1**) and the IPF maps in **Figure 11** (**a2-c2**) for NiCoCrMoCu alloy with various cold forged compression with reduction rates of (a1 and a2) 0%, (b1 and b2) 30%, and (c1 and c2) 60%. Alloy with defect-free grains exhibits a completely annealed microstructure, characterized by bright IQ values and a prevalence of continuous ∑3 annealing twinning boundaries, as indicated by the red lines in **Figure 11** (**a1**). And inverse pole figure (IPF) map (Figure 4 (a2)) reveals that in NiCoCrMoCu alloy without cold forged a structure of randomly distributed grains, without any obvious texture. After cold forged to 30%, the continuous ∑3 annealing twinning boundaries in **Figure 11** (**a1**) were partially divided into general grain boundaries, as indicated by the discontinuous red lines (**Figure 11** (**b1**)). In addition, slipping bands in the interior of grains are evident in the EBSD results (dashed lines in **Figure 11** (**b1**)) arrayed along the traces of the {111} planes. This indicates a predominance of dominant deformation through slipping in {111} planes, as shown in **Figure 11** (**b1**) for NiCoCrMoCu alloy. In addition, the grain lattice is slightly distorted, as evident by the color variation in the interior of grains in the IPF maps of alloys (**Figure 11** (**b2**)). After cold forged to 60%, the IQ map of NiCoCrMoCu-Cold60 sample displays darker contrast, indicating a more distorted matrix by deformation (**Figure 11** (**c1**)). The initial large grains become gradually subdivided into smaller parts with several micrometers in size by these deformation bands, which is indicative of a grain refining effect by cold working (**Figure 11** (**c1**)). The variation in the orientation color inside the grains also becomes more significant, implying greater distortion of the alloy matrix at higher compression reduction (**Figure 11** (**c2**)).

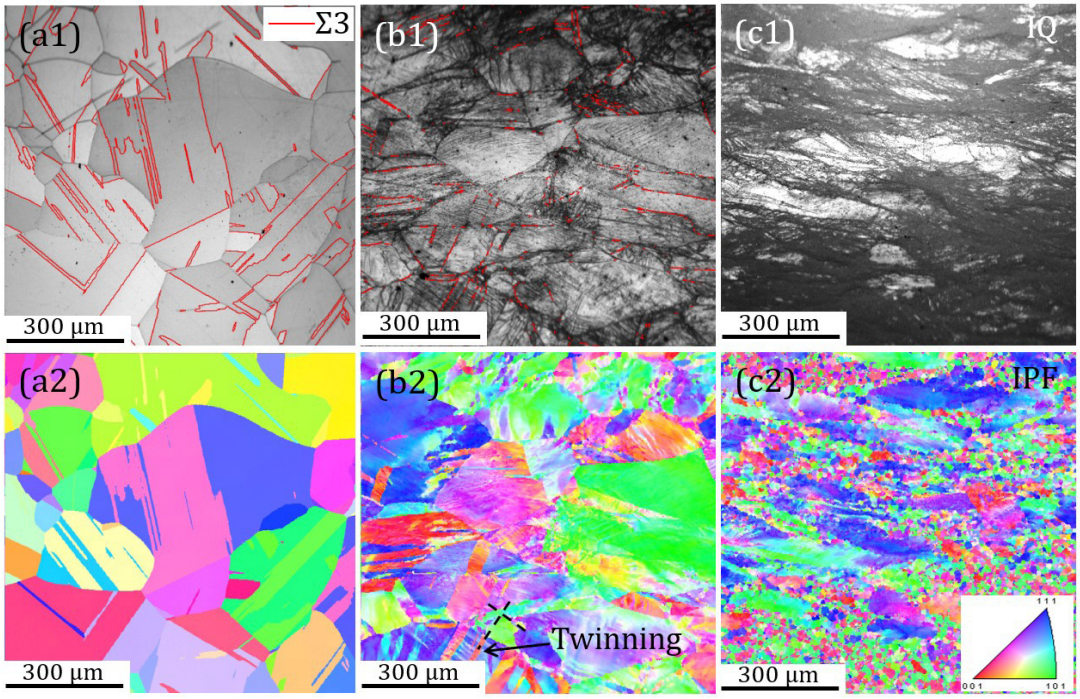

Figure 11: (a1–c1) IQ maps and (a2-c2) IPF maps of NiCoCrMoCu alloy cold forged to (a1 and a2) 0%, (b1 and b2) 30%, and (c1 and c2) 60%, respectively. Reprinted from ref.[21], with kind permission from Elsevier.

3.2.3. Corrosion performance of NiCoCrMo and NiCoCrMoCu alloys

After immersion tests in 5.2 M HF acid solution at 100°C for 100 h, the weight loss of NiCrMo, NiCoCrMo, and NiCoCrMoCu alloys under various deformation states are measured and their weight loss rates are shown in **Figure 12**. For one thing, for alloy with similar compositions, the more serious deformation being applied, the more severe corrosion occurs after immersion tests. For another thing, under comparable state for alloy, NiCoCrMoCu alloy shows the lowest weight loss after immersion tests, suggesting the addition of 2 wt.% Cu exerts a key role on improving the corrosion resistance of alloy in HF acid environment.

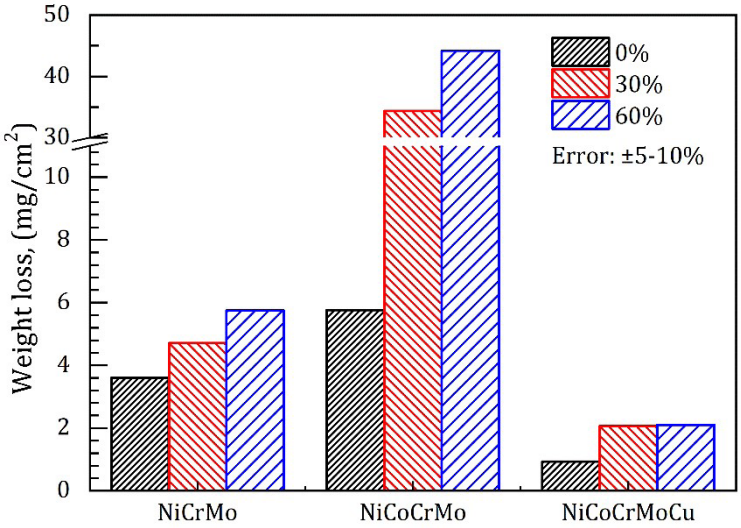

Figure 12: Weight losses of NiCrMo, NiCoCrMo, and NiCoCrMoCu alloys with a reduction rate of 0%, 30%, and 60% after immersion in 5.2 M HF acid aqueous solution at 100°C for 100 h.

3.2.4. Corrosion morphologies of NiCoCrMo and NiCoCrMoCu alloys

Laser scanning microscopy was used to observe the corroded surface of the samples, with **Figure 13** demonstrating the morphologies of NiCoCrMo and NiCoCrMoCu sample surfaces after immersion for 100 h with a similar cold forged compression of 60% reduction rate. Compared to NiCoCrMoCu-Cold60 sample, the NiCoCrMo-Cold60 sample surface becomes darker and heavily corroded as a result of the complete structural failure of the sample, as evidenced by its broken small pieces. Relative height distributions for the surfaces of both samples after immersion for 100 h are also displayed along the lines in **Figure 13**. From **Figure 13**, the NiCoCrMo-Cold60 sample surface is characterized by a large variation in surface height (2.5 μm) that is mostly concentrated within the vicinity of either grain boundaries or deformation bands, thus indicating significant local corrosion in this alloy. In contrast, NiCoCrMoCu-Cold60 sample shows less drastic variation in surface height, with its maximum variation of less than 0.8 μm implying that local corrosion is reduced in NiCoCrMoCu-Cold60 sample compared to NiCoCrMo-Cold60 sample.

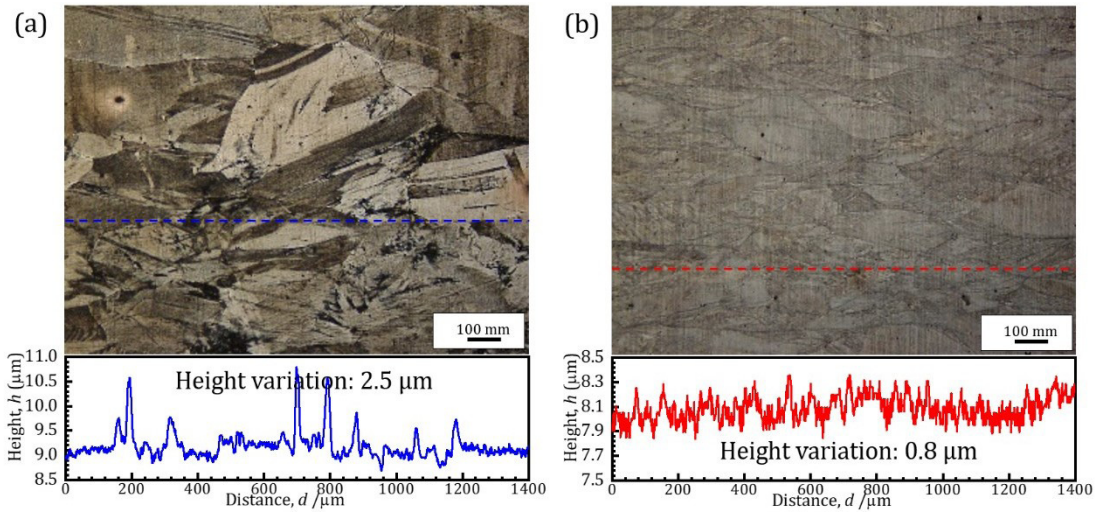

Figure 13: Surface morphologies and corresponding height distributions of the sample surface along the horizontal dashed lines in (a) NiCoCrMo-Cold60, and (b) NiCoCrMoCu-Cold60 specimens after immersion in 5.2 M HF acid aqueous solution at 100°C for 100 h.

3.2.5. XPS analysis of passive film

The Ni 2p, Co 2p, Cr 2p, Mo 3d, and Cu 2p spectra of the same samples recorded at a higher resolution are used to elucidate the chemical states of the elements, as shown in **Figure 14** (**a-e**), respectively. The spectral peaks are deconvoluted to show the contributions of metallic and fluoride or oxide states[52]. The acquired spectra include complex information. For example, in the NiCoCrMo sample, Cr and Co in both oxide and fluoride states are clearly detected, while no metallic peak is apparent, implying their high tendency to react with HF solution. Regarding Mo, Mo^{4+}, Mo^{5+}, and Mo^{6+} could be identified in the NiCoCrMo sample, while no Mo is detected in the metallic state. It is difficult to distinguish whether Ni and Mo exist in the oxide or fluoride state because of the insufficient XPS database available at present[52]. Nevertheless, by considering the low chemical stability and high solubility in

water of molybdenum fluorides (MoF_x, x = 4, 5, 6) as well as the fact that the intensities of O peaks are much higher than those of F, it is speculated that most of the Mo^{x+} exists in the form of oxides ($MoO_{x/2}$, x=4, 5, 6) [53–55]. After adding 2 wt.% Cu, the sample surface shows significantly different profiles in these spectra; most of the Ni, Co, Cr, and Mo are observed to be metallic states, while only small fractions of Cr and Mo are observed to exist in fluoride or oxide states, respectively. The spectrum of Cu on the sample surface is observed to exist at a binding energy of 932.8 eV, which is subtly higher than that in metallic states (932.6 eV) but much lower than that of Cu^{2+} 2p (944 eV), suggesting that Cu on the sample surface is dominantly composed of a metallic state together with some Cu^{1+} in the form of Cu_2O.

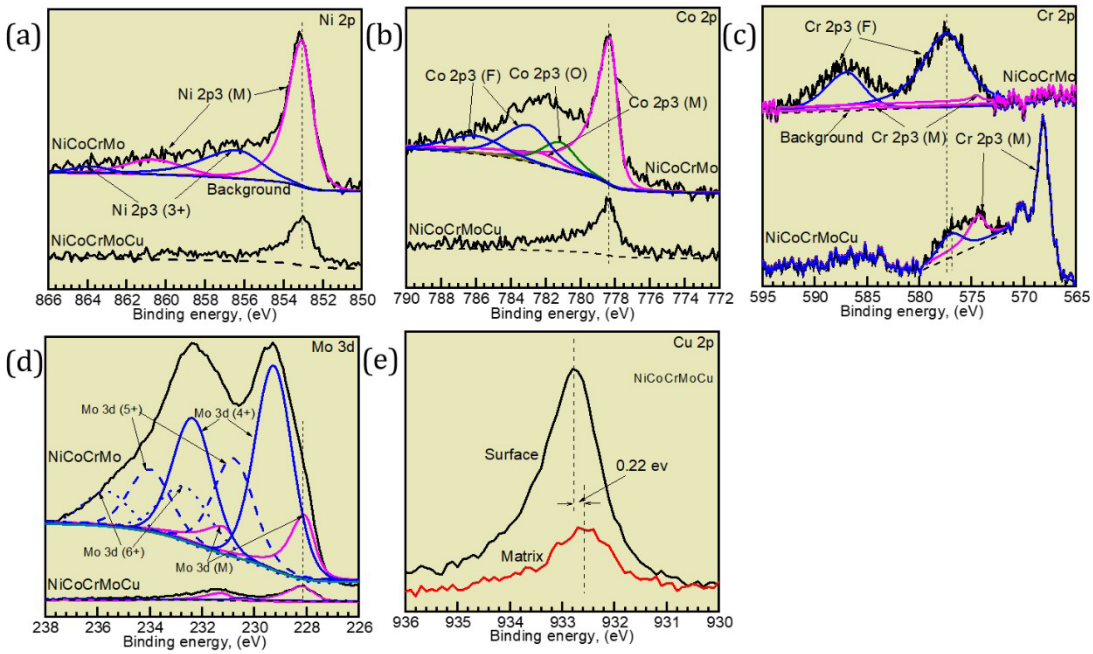

Figure 14: XPS regional scan spectra acquired from the outermost surfaces of the NiCoCrMo and NiCoCrMoCu samples after immersion in 5.2 M HF acid aqueous solution at 100°C for 100 h. The spectra corresponding to (a) Ni 2p, (b) Co 2p, (c) Cr 2p, (d) Mo 3d, and (e) Cu 2p are shown. Reprinted from ref. [51], with kind permission from Elsevier.

The spectra of the aforementioned elements (Ni, Co, Cr, Mo, and Cu) from the surfaces of both samples for various sputtering times with Ar gas are shown in **Figure 15**. The spectra are labelled by the sputtering time (s) on the probed area of the film. Significant peaks of non-metallic Ni, Co, Cr, and Mo are observed for sputtering times of 0 to approximately 180 s. Beyond 180 s, a gradual transition from the non-metallic peak to a metallic peak is observed. Among these elements, the peaks of Mo^{4+} are observed to be the strongest. In NiCoCrMoCu sample, a transition behavior similar to that of NiCoCrMo sample in the peaks of Ni, Co, and Cr is observed, while these peaks are much weaker for a sputtering time less than 180 s (**Figure 15**). The Cu 2p peak is observed to be the strongest in the film and is about several tens of times stronger than that in the matrix, confirming the significant segregation of Cu, rather than Mo, in the passive film of NiCoCrMoCu sample.

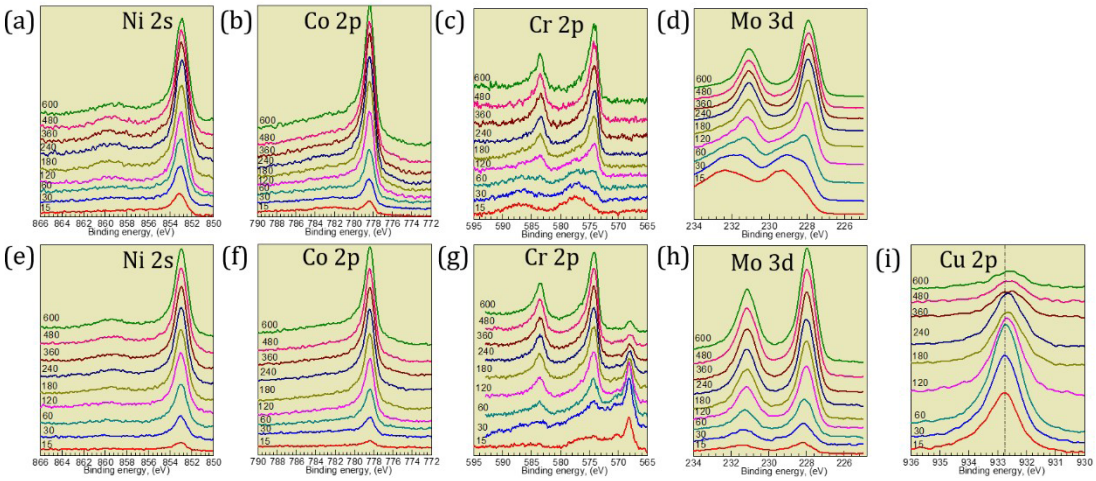

Figure 15: XPS spectra of (a, e) Ni 2s, (b, f) Co 2p, (c, g) Cr 2p, (d, h) Mo 3d and (i) Cu 2p (only in NiCoCrMoCu alloy) with various sputtering times for the (a-d) NiCoCrMo and (e-i) NiCoCrMoCu alloys after immersion in 5.2 M HF acid aqueous solution at 100°C for 100 h. Reprinted from ref. [51], with kind permission from Elsevier.

The fractions of Ni, Co, Cr, Mo, and Cu and their corresponding oxides and fluorides at various depths of the films of the two alloys are calculated from the Ni 2p, Co 2p, Cr 2p, Mo 3d, and Cu 2p peaks (**Figure 16**), respectively. For a comparison between the constitutions of the passive film and alloy matrix, O and F are not taken into consideration during the calculations. As expected, after immersion for 100 h, the passive films of the two samples are observed to be significantly different in that the passive film of NiCoCrMo alloy is dominated by Mo oxides, while that of NiCoCrMoCu is dominated by Cu. The atomic fractions of these two elements in the two films are observed to be higher than 50 mol.% at the outermost surface. In addition to Cu, the passive film of the NiCoCrMoCu alloy contains remnant metallic Ni, Cr, Co, and Mo. In contrast, apart from the dominant Mo oxides, the passive film in NiCoCrMo sample contains a large fraction of Ni^{3+}, Co^{2+}, and Cr^{3+}. The passive films of the two samples are of comparable thicknesses.

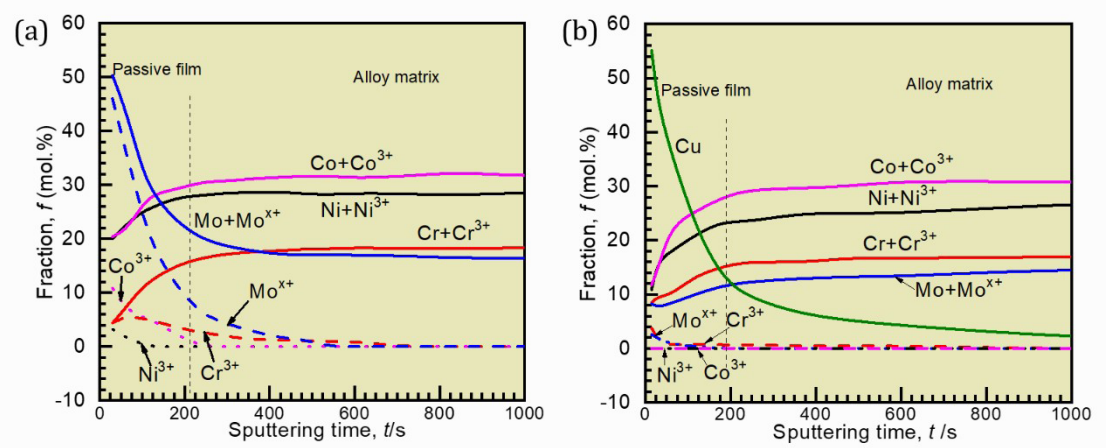

Figure 16: Atomic fractions of Ni, Co, Cr, Mo, and Cu in various states as a function of sputtering time calculated from XPS spectra for the samples after immersion in 5.2 M HF acid aqueous solution at 100°C for 100 h: (a) NiCoCrMo and (b) NiCoCrMoCu alloys. Reprinted from ref.[51], with kind permission from Elsevier.

The change in the composition of metallic elements from the matrix to the passive films demonstrate that during immersion, Ni, Co, and Cr dissolve in the HF solution through the formation of fluorides or oxides, while Mo and its oxides aggregate on the NiCoCrMo sample surface, acting as a barrier to HF infiltration. In NiCoCrMoCu sample, Cu aggregates on sample surface to form the passive film, which is more stable and more inert to HF solution, as is evident from the mass losses of the two alloys shown in **Figure 12**.

3.2.6. STEM-EDS elemental mapping of passive film

From the STEM-EDS mappings of NiCoCrMo samples in **Figure 17**, it is clear that the passive film is approximately 20 nm in depth and is slightly rich in both Mo and O, and the concentrations of other elements are a little lower. In the NiCoCrMoCu sample, the passive film is rich in Cu, and the O intensity is slightly higher than that of the matrix. It is worth noting that Mo, which is the dominant component in the NiCoCrMo alloy, is almost completely replaced by Cu in the film, although its concentration in the matrix is low.

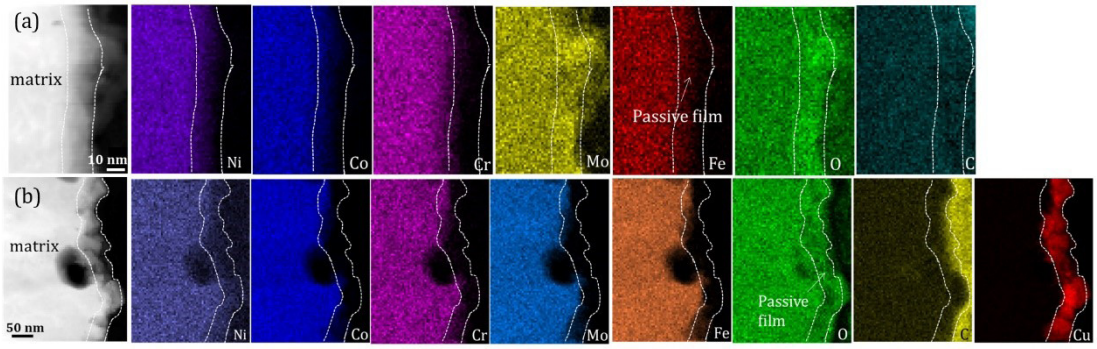

Figure 17. STEM images and corresponding EDS elemental mappings in the cross section of the passive film of (a) NiCoCrMo alloy for Ni, Co, Cr, Mo, Fe, O, and C, and (b) NiCoCrMoCu alloy for Ni, Co, Cr, Mo, Fe, O, C, and Cu after immersion in HF acid aqueous solution (5.2 M) at 100°C for 100 h. Reprinted from ref. [51], with kind permission from Elsevier.

3.2.7. Calculated Pourbaix diagrams

The Pourbaix diagrams for all metallic elements investigated in 5.2 M HF acid solution at 100°C calculated by HSC Chemistry 7.0 software are shown in **Figure 18**[56]. The pH value of 5.2 M HF solution can be estimated to be 0.222 based on the ionization constant of HF of about 6.8×10^{-2}[52]. The practical E-pH condition for the immersion tests can be roughly located in pH values of -2 to 1 and E_{SHE} of -0.4 to 0.2 V based on the weak acidity of HF and high temperature environment. Obviously, Co and Ni show comparable corrosion potential, suggesting that the substitution of Co for Ni has little influence on the corrosion behavior of alloy thermodynamically speaking. Another thing can be obtained from **Figure 18** is that Cu possesses the highest corrosion potential compared to other elements; Cu can exist stably in metallic state, suggesting its exceptional stability in HF solution. In other words, the addition of Cu to NiCoCrMo alloy is conducive to improve the corrosion resistance in HF solution.

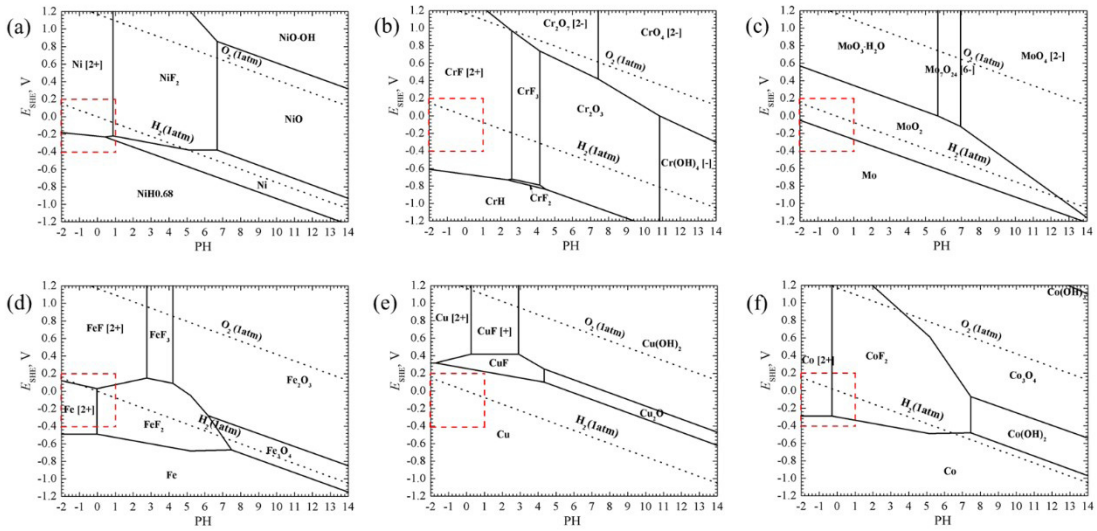

Figure 18. Pourbaix diagrams for metallic (a) Ni, (b) Cr, (c) Mo, (d) Fe, (e) Cu, and (f) Co in 5.2 M HF acid aqueous solution at 100°C calculated by HSC Chemistry 7.0 software. Reprinted from ref.[41], with kind permission from Elsevier.

3.2.8. Roles of aging treatments on NiCoCrMoCu alloys

Tensile tests were conducted on NiCoCrMoCu alloys subjected to various treatments, and corresponding results can be seen in **Figure 19**. From that, NiCoCrMoCu sample after hot forged shows the largest engineering strain higher than 40%, while further aging at 600°C for 1 h seems to be detrimental to both engineering strength and engineering strain. In contrast to hot forged samples, under comparable reduction of 60%, NiCoCrMoCu-Cold60 sample exhibits higher engineering strength and reduced engineering strain. NiCoCrMoCu-Cold90 sample shows evident improvement on engineering strength than NiCoCrMoCu-Cold60 sample. Further aging treatment on alloys after cold forged deformation further increases engineering strength while concurrently lowers engineering strain.

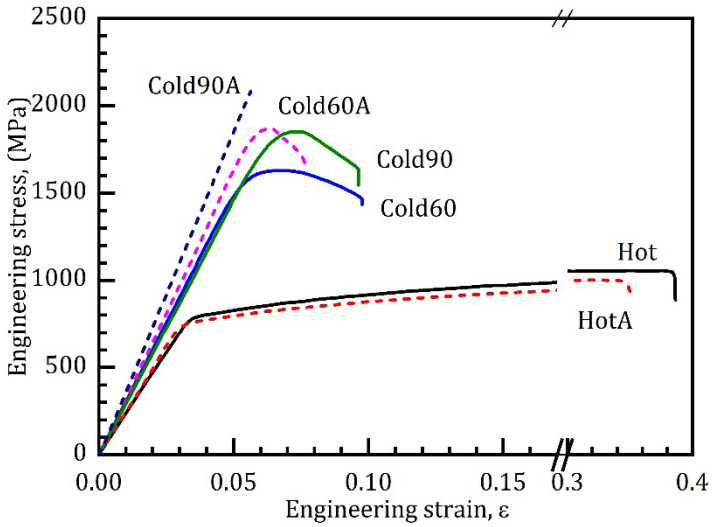

Figure 19: Tensile tests of NiCoCrMoCu samples after various processing treatments. Hot: Hot forging, Cold: cold forging, A: Aging, 600°C, 1h. Detailed nomination rules can be seen in Section 2.1.

A brief summary of (a) weight loss after corrosion and (b) hardness of aforementioned NiCoCrMoCu alloys and NiCrMo alloys are depicted in **Figure 20**. Obviously, NiCoCrMoCu alloys still possess excellent corrosion resistance to HF acid solution even after severe deformation and aging treatments. In the view of hardness, compared to NiCrMo alloys, NiCoCrMoCu alloys show extremely high hardness. For example, NiCoCrMoCu-Cold90A sample possesses the highest hardness of near 700 HV.

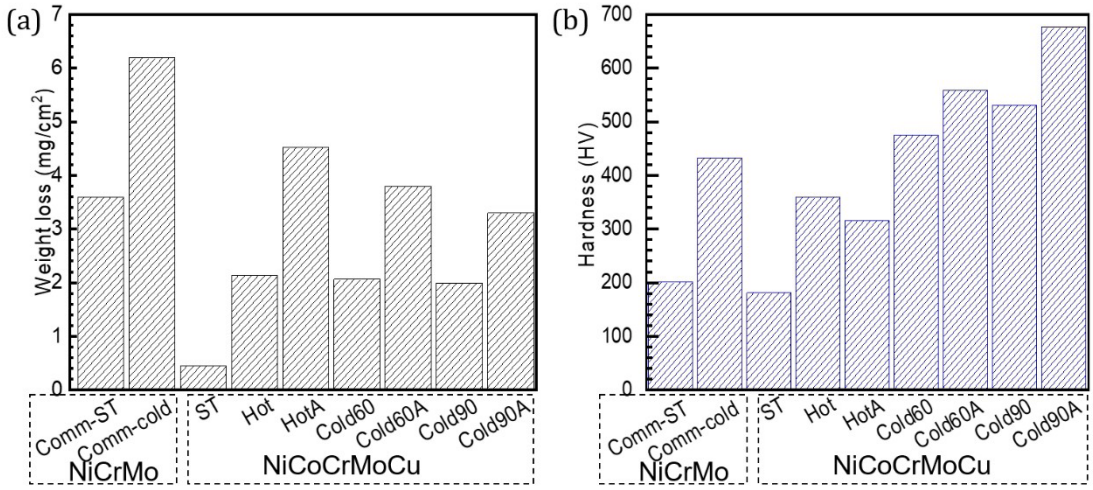

Figure 20 (**a**): Weight losses of samples subjected to various processing treatments. in 5.2 M HF acid aqueous solution at 100°C for 100 h, and (b) hardness results of NiCrMo and NiCoCrMoCu. ST: Solution treatment.

4. Conclusion and Outlook

Based on presently existing data, an Ashby plot depicting the mechanical performance and weight loss after corrosion tests of NiCrMo, NiCoCrMo, and NiCoCrMoCu alloys is drawn as **Figure 21**. Three states for every alloy are shown in this plot: casting, cold forged, and further aging treatment. Under casting state, NiCoCrMoCu alloy shows the most superior corrosion resistance to HF acid environment. And 60% cold forged deformation can introduce enormous dislocations in alloys, which thus boost the hardness of alloy by work hardening; meanwhile, the corrosion resistance of alloys seems to be lowered by the presence of defects after deformation. As we have discussed in section 3. 1, Co-bearing alloy shows many distinct and heterogenous deformation bands, resulting in severe galvanic corrosions and greatly decrease of corrosion resistance. Thus, NiCoCrMo alloy after 60% cold forged shows significant increase on weight loss rate although such alloy possesses higher hardness than NiCrMo alloy after 60% cold forged. By dual-alloying of 30 wt.% Co and 2 wt.% Cu, a novel NiCoCrMoCu alloy is obtained and such alloy subjected to 60% cold forged and subsequent aging at 600°C for 1 h exhibits both superior mechanical performance with hardness near 600 HV and excellent corrosion resistance to HF acid solution with a weight loss of appropriately 1 mg/cm^2.

In brief, a novel NiCoCrMoCu alloy with outstanding mechanical performance and corrosion resistance in HF aqueous acid solution is designed, however, there still exists several problems waiting to be addressed. Firstly, although the design of NiCoCrMoCu alloy based on

the rules of phase diagram, etc., it's still not very systematic. Only NiCoCrMoCu alloy with 30 wt.% Co and 2 wt.% Cu was designed and analyzed. How about other combinations of Co and Cu concentrations? It's still known until we design a series of NiCoCrMoCu alloys with various combinations of Co and Cu elements. Secondly, the addition of 30% Co to NiCrMo alloy has been determined to lower the stacking faults energy of alloy, increase the hardness of alloy. However, the deformation mechanism of NiCoCrMo alloy is still unknown. Thus, further deformation mechanism analysis of NiCoCrMo and NiCoCrMoCu alloys is imperative and meaningful.

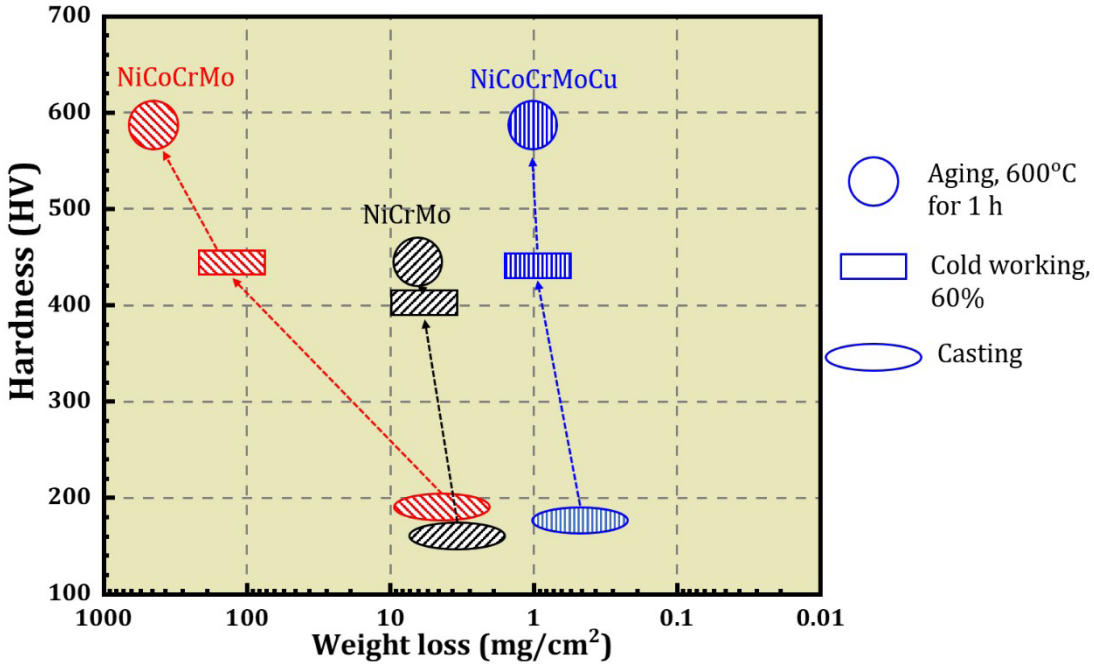

Figure 21: Performance summaries of NiCrMo, NiCoCrMo, and NiCoCrMoCu alloys under various states.

In spite of these two drawbacks, this chapter has succeeded to complete the design of a novel NiCoCrMoCu alloy with both superior mechanical performance and corrosion performance in HF aqueous acid solution. Through alloying, thermomechanical processing and microstructure controlling, extraordinary balanced tensile properties and corrosion performance were achieved. The complex corrosion mechanisms are also discussed systemically. The current work is a successful demonstration of using alloying and various strengthening approaches to manipulate the properties of Ni-based alloys, and the resulting findings are important not only for understanding the corrosion mechanisms of metallic materials in HF acid solution, but also for the future development of high-performance alloys for industrial applications.

5. Reference

1. Del Cul GD, Icenhour AS, Simmons DW. Prototype Tests for the Recovery and Conversion of UF6 Chemisorbed in NaF Traps for the Molten Salt Reactor Remediation Project. Oak Ridge National Lab., TN (US); 2000.

2. Zhou W, Woller KB, Zheng G (Tony), Stahle PW, Short MP. A simultaneous corrosion/irradiation facility for testing molten salt-facing materials. Nucl Instrum Methods Phys Res Sect B Beam Interact Mater At 2019;440:54–9.

3. Aigueperse J, Mollard P, Devilliers D, Chemla M, Faron R, Romano R, et al. Fluorine Compounds, Inorganic. Ullmanns Encycl. Ind. Chem., American Cancer Society; 2000.

4. Critchlow GW, Litchfield RE, Sutherland I, Grandy DB, Wilson S. A review and comparative study of release coatings for optimised abhesion in resin transfer moulding applications. Int J Adhes Adhes 2006;26:577–99.

5. Gong X, Cui Y, Wei D, Liu B, Liu R, Nie Y, et al. Building direction dependence of corrosion resistance property of Ti–6Al–4V alloy fabricated by electron beam melting. Corros Sci 2017;127:101–9.

6. Yu B, Li Y, Nie Y, Mei H. High temperature oxidation behavior of a novel cobalt-nickel-base superalloy. J Alloys Compd 2018;765:1148–57.

7. Yu B, Li Y, Lei Q, Nie Y. Microstructures and mechanical properties of WC-Co-xCr-Mo cement carbides. J Alloys Compd 2019;771:636–42.

8. Zhang X, Li Y, Tang N, Onodera E, Chiba A. Corrosion behaviour of CoCrMo alloys in 2 wt% sulphuric acid solution. Electrochimica Acta 2014;125:543–55.

9. Davis JR. Nickel, Cobalt, and Their Alloys. ASM International; 2000.

10. Li L, Gong X, Ye X, Teng J, Nie Y, Li Y, et al. Influence of Building Direction on the Oxidation Behavior of Inconel 718 Alloy Fabricated by Additive Manufacture of Electron Beam Melting. Materials 2018;11:2549.

11. Ye X, Li Y, Ai Y, Nie Y. Novel powder packing theory with bimodal particle size distribution-application in superalloy. Adv Powder Technol 2018;29:2280–7.

12. Yuan Y, Gu Y, Cui C, Osada T, Zhong Z, Tetsui T, et al. Influence of Co content on stacking fault energy in Ni–Co base disk superalloys. J Mater Res 2011;26:2833–7.

13. Yuan Y, Gu Y, Cui C, Osada T, Yokokawa T, Harada H. A Novel Strategy for the Design of Advanced Engineering Alloys—Strengthening Turbine Disk Superalloys via Twinning Structures. Adv Eng Mater 2011;13:296–300.

14. Xu H, Zhang ZJ, Zhang P, Cui CY, Jin T, Zhang ZF. The synchronous improvement of strength and plasticity (SISP) in new Ni-Co based disc superalloys by controling stacking fault energy. Sci Rep 2017;7:8046.

15. Chowdhury P, Sehitoglu H, Abuzaid W, Maier HJ. Mechanical response of low stacking fault energy Co–Ni alloys – Continuum, mesoscopic and atomic level treatments. Int J Plast 2015;71:32–61.

16. Hou Y, Li Y, Wang F, Zhang C, Koizumi Y, Chiba A. Influence of Mo concentration on corrosion resistance to HF acid solution of Ni–Co–Cr–Mo alloys with and without Cu. Corros Sci 2015;99:185–93.

17. Ujiro T, Satoh S, Staehle RW, Smyrl WH. Effect of alloying Cu on the corrosion resistance of stainless steels in chloride media. Corros Sci 2001;43:2185–200.

18. Ogura S, Sugimoto K, Sawada Y. Effects of Cu, Mo and C on the corrosion of deformed 18Cr8Ni stainless steels in H2SO4/NaCl solutions. Corros Sci 1976;16:323-330,IN9-IN12,331-337.

19. Seo M, Hultquist G, Leygraf C, Sato N. The influence of minor alloying elements (Nb, Ti and Cu) on the corrosion resistivity of ferritic stainless steel in sulfuric acid solution. Corros Sci 1986;26:949–60.

20. Sandoz G. The effects of alloying elements on the susceptibility to stress-corrosion cracking of martensitic steels in salt water. Metall Trans 1971;2:1055–63.

21. Zhang C, Li Y, Hou Y, Tang N, Ohmura K, Koizumi Y, et al. Corrosion resistance of Cu- and Fe-modified Ni–30Co–16Cr–15Mo alloy in aqueous hydrofluoric acid. Corros Sci 2014;89:81–92.

22. Lima HMLF de, Tavares SSM, Martins M, Araújo WS. The effect of copper addition on the corrosion resistance of cast duplex stainless steel. J Mater Res Technol 2019.

23. Wang F, Xiong B, Zhang Y, Liu H, Li Z, Li X, et al. Effect of Cu addition on microstructure and corrosion behavior of spray-deposited Zn–30Al alloy. Mater Sci Eng A 2012;532:100–5.

24. Xu Q, Gao K, Lv W, Pang X. Effects of alloyed Cr and Cu on the corrosion behavior of low-alloy steel in a simulated groundwater solution. Corros Sci 2016;102:114–24.

25. Yang B, Li J, Gong X, Nie Y, Li Y. Effects of Cu addition on the corrosion behavior of NiCoCrMo alloys in neutral chloride solution. RSC Adv 2017;7:40779–90.

26. Yang B, Shi C, Li Y, Lei Q, Nie Y. Effect of Cu on the corrosion resistance and electrochemical response of a Ni–Co–Cr–Mo alloy in acidic chloride solution. J Mater Res 2018;33:3801–8.

27. Rebak RB, Dillman JR, Crook P, Shawber CVV. Corrosion behavior of nickel alloys in wet hydrofluoric acid. Mater Corros 2001;52:289–97.

28. Osborne PE, Icenhour AS, Cul GDD. Hydrofluoric Acid Corrosion Study of High-Alloy Materials. 2002.

29. Kulkarni AJ, Krishnamurthy K, Deshmukh S, Mishra RS. Effect of Particle Size Distribution on Strength of Precipitation-hardened Alloys, 2004.

30. Sun YQ, Hazzledine PM. A TEM weak-beam study of dislocations in γ' in a deformed Ni-based superalloy. Philos Mag A 1988;58:603–17.

31. Zhang HY, Zhang SH, Cheng M, Zhao Z. Microstructure evolution of IN718 alloy during the delta process. Procedia Eng 2017;207:1099–104.

32. Ghosh S, Yadav S, Das G. Study of standard heat treatment on mechanical properties of Inconel 718 using ball indentation technique. Mater Lett 2008;62:2619–22.

33. Hou Y, Li Y, Zhang C, Koizumi Y, Chiba A. Effects of cold working on corrosion resistance of Co-modified Ni–16Cr–15Mo alloy in hydrofluoric acid solution. Corros Sci 2014;89:258–67.

34. Li Y, Fan X, Tang N, Bian H, Hou Y, Koizumi Y, et al. Effects of partially substituting cobalt for nickel on the corrosion resistance of a Ni–16Cr–15Mo alloy to aqueous hydrofluoric acid. Corros Sci 2014;78:101–10.

35. Thermo-Calc Software - Computational Materials Engineering n.d. https://www.thermocalc.com/ (accessed May 30, 2019).

36. Shkatulyak N. Effect of Stacking Fault Energy on the Mechanism of Texture Formation during Alternating Bending of FCC Metals and Alloys. Int J Nonferrous Metall 2013;02:35–40.

37. Li Y, Wu S, Bian H, Tang N, Liu B, Koizumi Y, et al. Grain refinement due to complex twin formation in rapid hot forging of magnesium alloy. Scr Mater 2013;68:171–4.

38. Li Y, Suzuki T, Tang N, Koizumi Y, Chiba A. Microstructure evolution of SUS303 free-cutting steel during hot compression process. Mater Sci Eng A 2013;583:161–8.

39. Olson GB, Cohen M. A general mechanism of martensitic nucleation: Part I. General concepts and the FCC → HCP transformation. Metall Trans A 1976;7:1897–904.

40. Olson GB, Cohen M. A general mechanism of martensitic nucleation: Part II. FCC → BCC and other martensitic transformations. Metall Trans A 1976;7:1905–14.

41. Yang B, Shi C, Teng J, Gong X, Ye X, Li Y, et al. Corrosion behaviours of low Mo Ni-(Co)-Cr-Mo alloys with various contents of Co in HF acid solution. J Alloys Compd 2019;791:215–24.

42. Miodownik AP. The calculation of stacking fault energies in Fe-Ni-Cr alloys. Calphad 1978;2:207–26.

43. Ye X, Yu B, Gong X, Yang B, Nie Y, Li Y, et al. Microstructure refining of Co-29Cr-6Mo-0.16N alloy in rapid hot-forging process. Mater Sci Eng A 2018;729:48–52.

44. Tunthawiroon P, Li Y, Koizumi Y, Chiba A. Strain-controlled iso-thermal fatigue behavior of Co–29Cr–6Mo used for tooling materials in Al die casting. Mater Sci Eng A 2017;703:27–36.

45. Li Y, Koizumi Y, Chiba A. Dynamic recrystallization in biomedical Co-29Cr-6Mo-0.16N alloy with low stacking fault energy. Mater Sci Eng A 2016;668:86–96.

46. Li Y, Li J, Koizumi Y, Chiba A. Dynamic recrystallization behavior of biomedical Co-29Cr-6Mo-0.16N alloy. Mater Charact 2016;118:50–6.

47. Anderoglu O, Misra A, Wang H, Ronning F, Hundley MF, Zhang X. Epitaxial nanotwinned Cu films with high strength and high conductivity. Appl Phys Lett 2008;93:083108.

48. Lu L. Ultrahigh Strength and High Electrical Conductivity in Copper. Science 2004;304:422–6.

49. Youssef K, Sakaliyska M, Bahmanpour H, Scattergood R, Koch C. Effect of stacking fault energy on mechanical behavior of bulk nanocrystalline Cu and Cu alloys. Acta Mater 2011;59:5758–64.

50. Hou Y, Li Y, Onodera E, Zhang C, Koizumi Y, Chiba A. Ex-situ observation on the dissolution behaviour of Ni–16Cr–15Mo and Ni–30Co–16Cr–15Mo alloys in hydrofluoric acid. Corros Sci 2015;90:133–9. doi:10.1016/j.corsci.2014.10.003.

51. Li Y, Xu X, Hou Y, Zhang C, Wang F, Omura K, et al. Regulating the passive film of NiCoCrMo alloy in hydrofluoric acid solution by small addition of Cu. Corros Sci 2015;98:119–27.

52. Moulder JF, Stickle WF, Sobol PE, Bomben KD. Handbook of X-ray photoelectron spectroscopy: a reference book of standard spectra for identification and interpretation of XPS data. Perkin-Elmer Corp 1992.

53. CRC Handbook of Chemistry and Physics, 99th Edition. CRC Press n.d. https://www.crcpress.com/CRC-Handbook-of-Chemistry-and-Physics-99th-Edition/Rumble/p/book/9781138561632 (accessed June 4, 2019).

54. Chase MW. NIST-JANAF Thermochemical Tables, 4th Edition | NIST. NIST-JANAF Thermochem Tables 2 Vol-Set J Phys Chem Ref Data Monogr 1998.

55. Drews T, Supel J, Hagenbach A, Seppelt K. Solid State Molecular Structures of Transition Metal Hexafluorides. ChemInform 2006;37.

56. HSC Chemistry, Software for Process simulation, Reactions Equations, Heat and Material Balances, Heat Loss Calculator, Equilibrium Calculations, Electrochemical Cell Equilibriums, Eh-pH Diagrams – Pourbaix diagram, Tpp Diagrams – Stability diagrams, Mineralogy Iterations n.d. http://www.hsc-chemistry.net/ (accessed June 4, 2019).